

Low variability, snowmelt runoff inhibits coupling of climate, tectonics, and topography in the Greater Caucasus

Expanded Methods and Figures

Adam M. Forte¹, Joel S. Leonard², Matthew W. Rossi³, Kelin X. Whipple², Arjun M. Heimsath², Lasha Sukhsvili⁴, Tea Godoladze⁴, and Fakhraddin Kadirov⁵

¹Department of Geology & Geophysics, Louisiana State University, Baton Rouge, LA, USA

²School of Earth and Space Exploration, Arizona State University, Tempe, AZ, USA

³Earth Lab, Cooperative Institute for Research in Environmental Sciences (CIRES), University of Colorado, Boulder, CO, USA

⁴Institute of Earth Sciences and National Seismic Monitoring Center, Ilia State University, Tbilisi, Georgia

⁵Institute of Geology and Geophysics of Azerbaijan National Academy of Sciences, Baku, Azerbaijan

Contents

1 Data Availability	2
2 Expanded Methods	2
2.1 ¹⁰ Be Sample Site Selection	2
2.2 ¹⁰ Be Sample Processing	2
2.3 Erosion Rate Calculation	3
2.4 Topographic, Tectonic, and Climatic Analysis	3
2.4.1 Basin Averaged Analyses	3
2.4.2 Convergence Gradient	4
2.5 Evaluating Influence of Lithology on Topography, Quartz Sourcing, and Erosion Rates	4
2.6 Fitting a Stream Power Incision Model Based Relationship Between k_{sn} and Erosion Rate	4
2.7 Discharge, Runoff, and Variability in the Caucasus in Gauged Basins	5
2.8 Estimating Hydroclimatic Parameters in Ungauged Basins	6
2.9 Application of the Stochastic Threshold Incision Model	6
2.9.1 Parameterization and Application of the STIM Relationship in the Caucasus	6
2.9.2 Comparison of SPIM and STIM Relationships	9
2.9.3 Cluster Analysis of STIM Relationship	9
3 Supplemental Table Captions	9
3.1 Table S1	9
3.2 Table S2	9
3.3 Table S3	10
4 Supplemental Figures and Captions	10

List of Figures

S1 GPS velocities	10
S2 χ -Z plots of sampled basins	11
S3 Quartz sourcing and erosion rates	11
S4 GPS velocity and erosion rates	12

S5	Spatial variation in erosion rates	12
S6	Topography and lithology comparisons for all basins	13
S7	Topography correlations	14
S8	Topography, gradient, erosion rate, and concavity	15
S9	Runoff and runoff variability in gauged basins	16
S10	Power law fit of data	17
S11	Channel width data from erosion rate basins	18
S12	Variation of optimized k_e , R and lithology	18
S13	k_{sn} , erosion rate, and optimized k_e and τ_c	19
S14	SPIM and STIM Residuals	19
S15	Cluster number selection	20
S16	Spatial distribution of clusters	20
S17	Clustered k_{sn} -E relationships and STIM relationships	21
S18	Predicted erosion rates from clustered and population wide STIM relationships	22
S19	Seasonal control on variability	23
S20	Rainfall and Runoff Time Series	24

1 Data Availability

The majority of the relevant data for the sample locations and associated data (e.g. gauged watersheds) are provided as tables included in the data repository. To aid in reproducibility and ease of usage, we also provide these data as text files in a GitHub repository. In this repository we also provide selected analysis scripts (these are highlighted in the supplemental methods document that follows), shapefiles, and rasters necessary to reproduce the analyses we present, along with a detailed description and figures related to the compiled lithology of each catchment. A complete list of the contents of the repository can be found in the ReadMe file in the repository.

2 Expanded Methods

2.1 ^{10}Be Sample Site Selection

Sample locations were pre-selected based on several criteria. We targeted basins with drainage areas between 5 - 100 km² and that did not include major knickpoints within their profiles or major variations in mean local relief (2500 m window) or normalized channel steepness (k_{sn}). The lower bound on drainage area was to avoid sampling extremely small catchments whose erosion rates can be significantly biased by landsliding events [Yanites et al., 2009, Niemi et al., 2005] and the upper bound was designed to avoid averaging over large spatial areas where erosion rates may vary due to tectonic heterogeneity (e.g. basins spanning across major structures, etc). We additionally avoided sampling catchments which included areas that were currently glaciated or had been glaciated during the last glacial maximum [Gobejishvili et al., 2011]. We attempted to select sample basins with minimal lithologic heterogeneity, but were limited by geopolitical constraints on possible sample locations. We also made an effort to sample across a wide range of mean annual rainfall rates and basin mean normalized channel steepness.

In the field, sample sites were evaluated for potential local landslide activity and human modification and when possible, we sampled river sediments upstream of settlements. Additionally, we attempted to sample tributaries at least 500 meters in elevation above their confluences with major trunk streams to avoid sampling reworked sediment that could have been deposited as a result of landslide dams on major streams. Sediment samples were preferentially taken from the active channels or bar deposits without vegetation. In total, we collected 76 samples (Table S2).

2.2 ^{10}Be Sample Processing

Of the 76 total samples, based on their spatial distribution, coverage of parameter space as defined by normalized channel steepness and mean annual precipitation rates, and additional field or topographic observations, we selected 47 samples to process for ^{10}Be . All samples were processed in the Surface Processes WOMBAT Laboratory in the School of Earth and Space Exploration at Arizona State University. Samples were wet sieved to 250-1000 μm and then air dried. All samples were cleaned in a 1:1 solution of HCl and HNO₃ at room temperature for 24 hours. Because of the abundance of quartz rich lithic clasts within the samples, initial attempts at standard HF and HNO₃ leaches to clean and concentrate quartz [e.g. Kohl and Nishizumi, 1992] were unsuccessful, and thus we needed to implement the much more labor and time intensive Hot Phosphoric Acid (HPA)

technique [Mifsud et al., 2013]. Through trial and error, we modified the original HPA technique to a three step process where in small (80g) aliquots of the sample were first boiled in a 50% solution of NaOH for 10-20 minutes, allowed to cool, and then washed thoroughly to decant off the fine grained residue. Then the remainder of the sample was slowly heated to 220°C in 80% orthophosphoric acid (H_3PO_4) to form pyrophosphoric acid ($H_4P_2O_7$) and then leached in this solution for 30-60 minutes. Finally, after cooling, the samples were washed thoroughly and boiled in another 50% solution of NaOH for 15-30 minutes and then, after cooling, washed and dried. The modified HPA technique was successful in removing the majority of feldspars and/or disaggregating lithic components present within the samples.

After the HPA, minerals denser than $2.85 \frac{g}{cm^3}$ were removed via lithium polytungstate (LST) density separation. To purify quartz in the remaining material, it was leached in 1-5% HF and HNO_3 solutions on heated rollers for at least 12 hours. Quartz yields for the majority of samples were very low (<5%), despite large masses (>1500g) of processed sample (Table S2). Of the original 47 samples, only 35 samples had sufficient quartz to proceed. Remaining quartz was spiked with either commercial or a low-background ^{9}Be carrier and digestions for purified quartz in HF and HNO_3 lasted for 7-10 days. Standard blank samples were processed along with each distinct batch of samples. We removed cations and anions using standard liquid chromatography techniques [Ditchburn and Whitehead, 1994]. Oxidized beryllium was mixed with a niobium matrix and loaded into cathodes for analysis at PRIME Lab, Purdue University. Beryllium isotope ratios for samples and blanks were referenced to isotope ratios defined in the 07KNSTD (Table S3). One sample (92715-2), which had been particularly problematic during the liquid chromatography steps, came back with 0 measured ^{10}Be , but spatially was surrounded by samples with very low erosion rates, thus we do not interpret this as a high erosion rate sample, but rather some sort of chemical processing error, and as such we exclude this from Table S3 and other subsequent results.

2.3 Erosion Rate Calculation

To calculate the catchment averaged erosion rates, we use the approach of Portenga and Bierman [2011], wherein for each basin we identify a single effective elevation, latitude, and longitude to approximate a suitable production rate of ^{10}Be for the entire basin. To accomplish this, we use topography for each basin from the Shuttle Radar Topography Mission (SRTM) 30-m digital elevation model and calculate a scaled ^{10}Be production rate based on the elevation and latitude of each pixel, using the production rate from spallation reactions using the scheme by Stone [2000]. From this, we calculate the mean production rate and then find the elevation and latitude (i.e. the effective latitude and elevation) within the basin that corresponds to this production rate. We use this effective latitude and elevation, along with the longitude of the centroid of the sampled basin and the calculated ^{10}Be concentrations in the online exposure age calculator formerly known as the CRONUS-Earth online exposure age calculator [Balco et al., 2008], v3.0 (accessed August 2019). Parameters used for erosion rate calculations are provided in Table S2. We assume no topographic shielding as this effect is usually small and has generally been shown to be unnecessary in steep landscapes [DiBiase, 2018]. We report erosion rates from all three schemes as reported by the calculator in Table S3, but elsewhere only use the time independent 'St' estimate using the scheme of Stone [2000].

2.4 Topographic, Tectonic, and Climatic Analysis

The analysis of topography, convergence rate, and basic climate variables largely follow prior efforts presented in Forte et al. [2014] and Forte et al. [2016]. We briefly review relevant methods in the following sections, focusing primarily on any updates from the original methodologies.

2.4.1 Basin Averaged Analyses

We use the Shuttle Radar Topography Mission (SRTM) 30 meter digital elevation model and a combination of TopoToolbox [Schwanghart and Scherler, 2014] and the Topographic-Analysis-Kit [TAK; Forte and Whipple, 2019] to calculate basin averaged statistics. For calculation of normalized channel steepness (k_{sn}), we use a reference concavity of 0.50, a smoothing length of 1000 m, the 'ksn_quick' method within TAK and for hillslope gradients we use the 'arcslope' method within the base TopoToolbox gradient8 function. We report a variety of basic topographic statistics and metrics, including elevation, k_{sn} (across a range of concavity values), gradient, and the best fit concavity and χR^2 for each basin (Table S3). The χR^2 statistic describes the extent to which the relationship between χ and elevation is linear. A steady state basin with no knickpoints should have a linear χ and elevation relationship and thus a χR^2 value close to 1. χR^2 values for basins generally are a better indicator of potential disequilibrium than either the standard deviation or standard error of the mean of k_{sn} as these metrics more reflect noise in the underlying DEM. All but two of the reported basins (16AF01 and 90216-1) have χR^2 values > 0.9, and χR^2 of trunk stream values > than 0.97, indicating the majority of these basins lack major knickpoints (Figure S2). The knickpoints in 16AF01 and 90216-1 are not extreme and neither of these basins represent outliers in k_{sn} or erosion rate space, thus we do not think that their inclusion in the analysis is inappropriate, however we evaluate their exclusion from the dataset in a later section.

2.4.2 Convergence Gradient

We follow the methodology discussed in Forte et al. [2014] in calculating along-strike gradients in convergence within the Greater Caucasus. The calculation uses the same original data used by Forte et al. [2014], but also includes additional stations and updated observations at some stations from Sokhadze et al. [2018]. As in Forte et al. [2014], we classified GSP stations as either being in the Lesser or Greater Caucasus, largely using the block boundaries defined by Reilinger et al. [2006] (Figure S4). We then use TAK [Forte and Whipple, 2019] to project the locations of these selected stations onto the swath along the crest of the Greater Caucasus so that they have a common reference frame with the erosion rate basins. For stations defined as 'Lesser Caucasus' or 'Greater Caucasus', we calculate a smoothed N25°E velocity by taking the average within a moving 50 km window which is interpolated over the along-strike length of main the swath (dashed lines in the bottom of Figure S1). We calculate similar moving averages for the extremes of both datasets using the uncertainty on the GPS velocities (shaded regions in the bottom of Figure S1). We then use similar assumptions as Forte et al. [2014] and difference the Lesser Caucasus and Greater Caucasus velocities. This difference is interpreted as an approximation of the amount of convergence along the southern margin of the Greater Caucasus, with the remaining velocity of the Greater Caucasus accommodated as convergence within the range or along its northern flank.

2.5 Evaluating Influence of Lithology on Topography, Quartz Sourcing, and Erosion Rates

To assess the potential role that lithology plays in influencing our results, either in terms of variable sourcing of quartz or topographic statistics, for each sampled catchment we digitized available geologic maps and compiled lithologic information. These complied geologic maps and details of the sources from which they were compiled are available in the GitHub repository. Using these digitized lithologic classifications, we then used the functionality within TAK [Forte and Whipple, 2019] to calculate the percent of each catchment occupied by specific lithologies, which are reported in Table S3. For each catchment, we produced explorative plots to assess whether the distribution of lithologies had meaningful contributions to the topographic metrics (i.e. k_{sn} and slope gradient). While many catchments exhibit at least some degree of correlation between values of k_{sn} or gradient and lithology, none of these patterns appear consistent, i.e. no particular lithology appears to always be steeper or shallower across catchments (Figure S6). The only lithologies that appear to have consistent k_{sn} or gradients, or values of either that differ substantially from the statistics of the population as a whole, are those which represent very small portions of the area and as such, we do not think this is diagnostic of the representation of a lithologic influence on topography, but rather a reflection of the topography of the specific catchments which include these lithologies.

More critically, given the documented extremely low quartz yields from all samples (e.g. Table S3), we also tested the sensitivity of the calculated erosion rates to variable quartz sourcing based on lithologic heterogeneity. We first recalculated appropriate latitudes and elevations for the production rate calculations again using the method of Portenga and Bierman [2011], but after filtering out portions of any catchments with dominantly carbonate lithologies, specifically those classified as 'limestone', 'limestone and marl', and 'marl'. We did not filter out 'limestone and minor clastics' and 'limestone and sandstone' as we assumed these units may still contribute sufficient quartz from their clastic constituents. We then used these updated elevation and latitude values in the online erosion rate calculator (Table S3) and paired this with mean basin k_{sn} values calculated excluding the same portions of each watershed. The calculated erosion rates, mean basin k_{sn} values, mean basin gradient, and pattern between erosion rates and either topographic metric was not appreciably different after filtering out these dominant carbonate lithologies (Figure S3)

Given the uncertainty in individual unit descriptions (and unknown quartz concentrations within the units), we additionally tested two end member schemes for calculation of production and erosion rates along with topography. For these schemes, we assumed that either all of the quartz was sourced from the bottom or top 50% of the catchment and calculated appropriate elevations and latitudes for use in the online calculator and topographic metrics for the respective portions of the catchments. Results from the erosion rate calculations are reported in Table S3. As with the lithological filtering, this experiment did not appreciably change the nature of the relationship between topography and erosion rate (e.g. Figure S3), thus generally we do not consider variable quartz sourcing as a source of uncertainty in the erosion rates and our subsequent conclusions.

2.6 Fitting a Stream Power Incision Model Based Relationship Between k_{sn} and Erosion Rate

To fit a stream power incision model (SPIM) based power law relationship between k_{sn} and erosion rate, we fit the available data using a bootstrap routine, which we describe below. We also fit the data using a monte-carlo scheme similar to Adams et al. [2020], but it produced estimates of the parameters within the uncertainty bounds of the bootstrap fit, so we do not discuss present results from these.

For the bootstrap approach, we use bootstrap sampling, i.e. random sampling of a N member dataset with replacement to produce a bootstrap sample also with N members, but that may have multiple repeated entries. Each bootstrap sample draws from a set of k_{sn} - erosion rate pairs with their respective uncertainties, i.e. the relationships between k_{sn} and erosion rate for particular samples are preserved in the bootstrap sampling process. An orthogonal distance regression fit (considering uncertainty) is performed on each bootstrap sample and this procedure is repeated an arbitrarily large number of times. Ultimately we are interested in the population of fit parameters, i.e. coefficients and exponents of the power law, and we can choose the most appropriate coefficient and exponent pair by finding the medians of these fit parameter populations. This bootstrap technique is explicitly designed to test the importance of outliers.

For each individual fit, we use the orthogonal distance regression (ODR) algorithm as implemented in SciPy and the k_{sn} - E relationship,

$$E = K(k_{sn})^n \quad (\text{S1})$$

as a log-transformed version such that it is a linear fit using,

$$\log_{10}(E) = n * \log_{10}(k_{sn}) + \log_{10}(K) \quad (\text{S2})$$

We perform 1e6 individual fits and then aggregate the population of fit parameters, i.e. values of K and n . We exclude data from sample 91416-1 for all fits because the uncertainty value for erosion rate is greater than the measured rate. We also perform a second set of fits where we exclude the two highest erosion rate basins (samples 90416-1 and 90216-2) and the two basins with lower χR^2 values (16AF01 and 90216-1, Figure S2) to estimate a more conservative set of parameters (Figure S10). We emphasize however that there is no specific reason to exclude the two high erosion rate samples, i.e. other than the erosion rate, there is nothing anomalous about these basins that cause us to question the validity of these rates.

For each population of fits, we use the median value (see bottom panel of Figure S10) of n and K to define the main curve. The shaded area is defined by the 25th and 75th percentile of the n and K values, specifically pairing the 25th percentile n with the 75th percentile K and vice versa. We use the median and quartile range because the bootstrap fit parameter distributions are skewed and thus the median and quartile range are less biased measures of the central tendency than the mean and standard deviation. Removing the two highest erosion rates and the two basins with some degree of disequilibrium does decrease the best bootstrap fit n value from 3.46 to 3.07 (primarily driven by the removal of the two high erosion rate basins), but (1) this lower n still implies a very nonlinear k_{sn} - erosion rate and thus does not appreciably change the result and (2) this lower median n is within the uncertainty bounds on the estimation of n from the fits that include these high erosion rate basins.

2.7 Discharge, Runoff, and Variability in the Caucasus in Gauged Basins

With our ultimate goal being the approximation of both mean runoff and runoff variability for the ungauged sampled ^{10}Be basins, we start with an analysis of gauged basins in the Caucasus region. Forte et al. [2016] presented such an analysis of available daily discharge data from gauged basins within the Caucasus region provided by the Global Runoff Data Centre (GRDC). Here, we use the same underlying dataset as Forte et al. [2016], but reprocess it to (1) describe variability with a power law right tail (i.e. inverse gamma, k) for use in equations related to the stochastic threshold incision model as in Forte et al. [2016], the tail of the discharge distributions were fit with a stretched exponential [e.g. Rossi et al., 2016] and (2) to remove potentially problematic basins from the dataset which may have anomalous discharges or variability. Specifically, using publicly available satellite imagery, we manually inspected the course of rivers within the GRDC basins and removed from the dataset any basins which had visible dams. As in Forte et al. [2016], we use a threshold of 99% to fit the tail of the discharge distribution. We provide a shapefile of the GRDC basins with relevant summary values in the attribute table in the GitHub repository.

To convert from discharge to runoff, we assume a simple relationship between drainage area and discharge,

$$Q = RA^c \quad (\text{S3})$$

where R is runoff, Q is discharge, and A is drainage area. We follow DiBiase and Whipple [2011] and assume $c = 1$, i.e. a linear relationship. This linear approximation appears valid, i.e. after accounting for spatial variation in rainfall rates, there is a quasi-linear relationship between discharge and drainage area (Figure 2). Results from this analysis are reported in Table S1. As discussed in the main text (and visible in Figure S9), the variability values are quite low (i.e. the k parameters are high). This is consistent with other analyses of runoff variability in the Caucasus region. Specifically Sutcliffe et al. [2008] analyzed a different, larger set of gauging stations and generally found low variability in runoff. More direct comparison of our results and

those presented in Sutcliffe et al. [2008] are challenging as they characterize the runoff with generalized extreme value theory using a block maxima approach (which is appropriate given that they had access to monthly or annual maxima as opposed to daily data) where as we use a peaks over threshold approach.

2.8 Estimating Hydroclimatic Parameters in Ungauged Basins

Mean Runoff To estimate mean daily runoff in the ungauged ^{10}Be sample basins, we use a spatially continuous rainfall dataset (TRMM 3B42) to estimate runoff in ungauged basins (Figure 3). We first account for differences between precipitation as estimated from ground based precipitation stations, which are more appropriate for comparison with runoff data but are spatially discontinuous, and rainfall estimates from satellite observations. We use precipitation station data from the European Climate and Assessment Dataset (ECAD) [Klein Tank et al., 2002] for this purpose as this covers the majority of the area of interest and individual station data has been vetted. A shapefile of the mean precipitation for the relevant ECAD stations are provided in the GitHub repository. The underlying TRMM data is the same as that presented in Forte et al. [2016], see this publication for details. For each ECAD station, we extract the mean values of the corresponding TRMM pixel and then fit a linear relationship to the resulting population (Figure 3), which can be used to bias correct the TRMM rainfall estimates.

After bias-correcting the TRMM data, we then calculate the mean basin rainfall within individual GRDC basins and then apply the correction to the TRMM data, which effectively shifts all of the rainfall to slightly lower magnitudes. From this, we then calculate the runoff ratio, i.e. $\frac{\bar{R}}{MDR}$, and fit a linear relationship between the runoff ratio and corrected mean basin rainfall (Figure 3). From this relationship, mean basin rainfall (as estimated from the corrected TRMM) for any watershed can be converted to an estimated runoff ratio and the estimated runoff can be found by multiplying the mean basin rainfall by this estimated runoff ratio. The application of this procedure to the ungauged ^{10}Be sample basins is presented in Table S3. It is worth noting that generally, gauged basins with mean runoffs below 3 mm/day have mean basin rainfall rates that are greater than their runoffs, i.e. the runoff ratio is below 1. However, consistently for basins above 3 mm/day of gauged runoff, the mean runoff exceeds the mean basin rainfall, i.e. the runoff ratio is greater than 1. Consequently, the result of the linear fit between runoff ratios and mean basin rainfall implies that any basin with a mean rainfall rate of 4 mm/day or greater would have a runoff ratio >1 . We expect that these runoff ratios >1 result from an underestimation of the precipitation within the TRMM 3B42 data. TRMM 3B42 data is specifically known to underestimate precipitation that falls as snow at high elevations [e.g. Wulf et al., 2016]. Correction of the TRMM using the ECAD station data was meant to partially offset general disagreements between station and satellite precipitation measures, but the ability of our correction is limited by assuming a linear relationship (with the caveat being that we do not think a higher order polynomial or alternate form is warranted given the scatter in the data) and the relative lack of ECAD stations at high elevations (e.g. Figure 3).

Runoff Variability To estimate runoff variability, we take a similar approach as for estimating mean daily runoff, i.e. relating observed runoff variability in gauged basins to a spatially continuous parameter that can be used to estimate runoff variability in ungauged basins. We tested the efficacy of a variety of topographic and climatic metrics for this purpose and found that the two best predictors of runoff variability were the maximum elevation of the gauged watershed and the basin mean of the standard deviation of monthly mean snow cover (Figure 4). This latter metric was used by Forte et al. [2016] as a proxy for the relative importance of snow melt in generating runoff. We provide a georeferenced raster of the standard deviation of monthly mean snow cover in the GitHub repository.

Applying the linear relationships between maximum elevation and the standard deviation of monthly mean snow cover from the gauged basins allows us to estimate the variability for ungauged basins, specifically the ^{10}Be sample basins. The results of both of these approximations are reported in Table S3. For subsequent analyses that require the variability, we use the average of these two estimates for each basin.

2.9 Application of the Stochastic Threshold Incision Model

2.9.1 Parameterization and Application of the STIM Relationship in the Caucasus

To apply the stochastic threshold incision model (STIM) to our data, we numerically solve for mean erosion rate \bar{I} using the version of STIM presented by DiBiase and Whipple [2011]:

$$\bar{I} = \int_{Q_c^*(k_s)}^{Q_m^*} I(Q^*, k_s) pdf_{\bar{Q}_k}(Q^*) dQ^* \quad (\text{S4})$$

where \bar{Q} is mean discharge, Q^* is normalized discharged such that $Q^* = Q/\bar{Q}$, Q_c^* is the minimum discharge that will overcome τ_c and Q_m^* is the maximum discharge observed within the considered time frame. In Equation S4, the instantaneous incision rate I is given by,

$$I = K \bar{Q}^m Q^{*\gamma} S^n - \Psi_c \quad (\text{S5})$$

where K is erosional efficiency, S is channel slope, Ψ_c is a threshold term, and m , n , and γ are empirical constants. In Equation S4, we follow Lague et al. [2005] and consider the probability distribution of discharge $pdf_{\bar{Q}_k}$, as

$$pdf_{\bar{Q}_k} = \frac{k^{k+1}}{\Gamma(k+1)} \exp\left(-\frac{k}{Q^*}\right) Q^{*(2+k)} \quad (\text{S6})$$

For a full derivation of these equations and a complete discussion of their terms, we refer readers to Lague et al. [2005] or DiBiase and Whipple [2011]. Our implementation of the STIM relationships are provided in the GitHub repository as *stochastic_threshold.py*.

From the prior results, for each erosion rate basin, we have estimates of the mean runoff and runoff variability (Table S3), but to explore the extent to which STIM relationship, considering these runoffs and variabilities, explains the observed patterns between ^{10}Be erosion rates and k_{sn} , we must assign, or estimate, values parameters within STIM. We list the values used and their associated units below:

Parameter	Value	Units
k_e	Variable	$m^{2.5} s^2 kg^{-1.5}$
R	Variable	$m^1 s^{-1}$
k	Variable	Dimensionless
τ_c	45	Pa
k_w	15	$m^{-0.5} s^{0.5}$
k_t	1000	$m^{-7/3} s^{-4/3} kg$
ω_a	0.5	Dimensionless
ω_s	0.25	Dimensionless
a	3/2	Dimensionless
α	2/3	Dimensionless
β	2/3	Dimensionless

We assume a Darcy-Weisbach friction relation and set $\alpha = \beta = 2/3$, follow Tucker [2004] and set $k_t = 1000$, such that $k_t = \rho_w g^{2/3} C_f^{1/3}$ where $C_f = 0.08313$, and we set $a = 3/2$, which assumes unit stream power. We do not have direct field observations with regards to channel width or cross sectional form, so for ω_s we use a value of 0.25 consistent with a concave channel cross section and between the expected range of 0 to 0.5 [Lague et al., 2005]. With $\omega_s = 0.25$, we set $\omega_a = 0.50$ so that the ratio of m/n , i.e. the concavity, equals 0.5 to be consistent with the reference concavity we use to calculate k_{sn} .

For k_w , which is the coefficient on the power law relationship between channel width, w , at a given discharge Q ,

$$w = k_w Q^{\omega_a} \quad (\text{S7})$$

we use a value of 15, which is the same value used by DiBiase and Whipple [2011]. To explore whether this choice of k_w is appropriate, it is necessary to compare the predictions for channel width implied by this value, along with the value of ω_a , to field measurements of width. In the absence of such field measurements, we use the 'ChanGeom' tool [Fisher et al., 2013], which can be used to measure channel widths on high resolution satellite imagery. Careful measurements using this tool have been shown to be similar to field measured widths in both the Himalaya and Taiwan [e.g. Fisher et al., 2013, Yanites et al., 2018]. Specifically, we use freely available imagery in Google Earth to map channel widths and the methodology of Yanites et al. [2018] in which we map the extent of largely vegetation free, gravel areas surrounding channels, with the assumption being that this represents areas which experience flows often enough to suppress the establishment of vegetation. Where clear edges of terraces into which this channel belt are cut, we use this as the edge of the channel. At larger drainage areas, this often represents a channel width that is significantly wider than the visible channel occupied by water in a single given satellite image.

The choice to map channels in this manner is in part based on field observations where these gravel areas are routinely inundated during higher flow events or after individual rain storms along with the variability in channel width and position (i.e. the width of the area occupied by water) observed in different satellite images taken over different years which are available within Google Earth. This means that some portion of the channel width measurements are biased towards widths largely relevant for discharges higher than the mean. In other areas, only the channel occupied by water is visible within the imagery, usually due to tree cover, so in these cases, we mapped this as the channel width. Together, our channel width measures are likely a mixture of widths relevant for mean discharges and those for higher, moderate flood discharges depending on local conditions and available imagery.

Using this methodology, we were able to measure channel widths for 26 of the 34 erosion rate basins. For the other 8 basins, the imagery available was insufficient to measure channel widths largely because the channels were completely obscured by tree cover. The results of these channel width measurements as a function of drainage area are presented in Figure S11. The underlying data for this plot and plotting algorithm are also provided in the GitHub repository.

We use the width estimates to evaluate the choice of $k_w = 15$ and $\omega_a = 0.5$, specifically by combining equation S3 and S7 to derive a relationship between width, runoff, and drainage area,

$$w = k_w R^{\omega_a} A^{\omega_a c} \quad (\text{S8})$$

We again assume $c = 1$ and use the discharge data for the gauged basins to calculate runoffs, R , at the mean discharge and a moderate flood, i.e. the discharge associated with the 2-year flood. We then evaluate this relationship at a series of reference drainage areas that span the areas within our measured width data. Comparisons between the predicted width-drainage area relationship and those measured suggest reasonable agreement, and thus that the choice of k_w and ω_a appear appropriate (Figure S11). At a given drainage area, the predicted widths also span much of the range of measured widths and further highlight that our measurements likely reflect a mixture of widths reflective of mean discharges and higher, moderate flood discharges. It is also worth highlighting that the lack of a clear relationship between channel width and mean basin erosion rate suggests that adjustment of channel width as opposed to slope is not a robust explanation for the $k_{\text{sn}}\text{-}E$ pattern in the Greater Caucasus. This analysis does assume there is no specific difference in the relations between width, drainage area, runoff, and discharge within the gauged basins compared (which we use to calculate the width for the mean and 2 year flood event) and the erosion rate basins (which we used to measure the widths). Given that we are already assuming some amount of correspondence between behavior in the gauged basins and erosion rate basins to estimate mean runoff and variability, we consider this appropriate.

This finally leaves estimation of k_e and τ_c , which together dictate the threshold term Ψ_c :

$$\Psi_c = k_e \tau_c^a \quad (\text{S9})$$

τ_c can be estimated from the grain size distribution within channels [e.g., DiBiase and Whipple, 2011], but we presently do not have (and are not aware of any published) estimates of grain size distributions for streams in the Greater Caucasus. In the absence of such grain size data, we first use a fixed τ_c of 45 Pa. Relating this back to grain size and using a Shields criterion with a critical Shields stress of 0.3 and densities for sediment (ρ_s) and water (ρ_w) densities of 2700 and 1000 kg*m⁻³ respectively [after DiBiase and Whipple, 2011],

$$\tau_c = 0.3(\rho_s - \rho_w)D_{50} \quad (\text{S10})$$

a τ_c of 45 Pa corresponds to a D_{50} of 90 mm. We consider this a reasonable approximation as this lies between the median (79 mm) and mean (107 mm) of the large compilation of D_{50} values from a variety of different types of steep mountain streams [e.g. Palucis and Lamb, 2017].

Fixing τ_c to 45 Pa, we then estimate acceptable ranges of k_e values. For each sampled basin, we use the assigned parameter values as described above, the estimated mean runoff and runoff variability, and the measured basin averaged k_{sn} , to find the k_e value for that basin that will best reproduce the measured basin averaged ¹⁰Be erosion rate. In this estimation, we also wish to account for the uncertainty on both basin averaged k_{sn} and erosion rate, so for each basin, we generate a synthetic set of k_{sn} and erosion rates drawn for a normal distribution centered on the observed value and with a standard deviation equal to the uncertainty. We then minimize the root mean squared error between these populations of synthetic erosion rates and erosion rates calculated from the STIM relationship using the corresponding population of synthetic k_{sn} . This results in a wide range of k_e values that have a quasi-linear relationship with estimated mean runoff, but not runoff variability (Figure 6). These estimated k_e values have no meaningful relationship with lithology (Figure S12). The algorithm to perform this optimization is provided in the GitHub repository as *optimize_k_e.py*.

2.9.2 Comparison of SPIM and STIM Relationships

Comparison of the best fit SPIM relationship from the bootstrap fitting, the SPIM relationship using the median values, or the best fit SPIM relationship all reveal similar residuals and root mean squared errors (Figure S14). Depending on whether residuals for k_{sn} or erosion rates are considered, either the SPIM or STIM have slightly better performance, at least using the RMSE as a determinant. In detail, for residuals on k_{sn} , both versions of the STIM are more uniform with respect to the residual values through a range of erosion rates, where as the SPIM has lower residuals for low k_{sn} -E pairs and higher residuals for high k_{sn} -E pairs (Figure S14 - top row). For residuals on erosion rates, the SPIM better matches the erosion rates at low k_{sn} ($<\sim 250$), where as STIM using the median values better matches the erosion rates at moderate to high k_{sn} (between ~ 375 -425) and both fail to meaningfully explain several samples. The algorithms to calculate a best fit using the STIM relationship (*stim.fit.py*) and calculate the RMSE and residuals (*residuals.py*) are provided in the GitHub repository.

2.9.3 Cluster Analysis of STIM Relationship

While this median STIM relationship qualitatively does reproduce the general shape of the observed k_{sn} - erosion rate relationship and some of the along-strike patterns in k_{sn} , this can be refined considering that there is a wide range in both mean runoff and runoff variability from our estimates. To investigate this, we identify populations within the basins as defined by the estimated mean runoff and variability using a k-means clustering analysis. The data was scaled prior to cluster analysis using the 'StandardScaler' in scikit-learn such that the mean of each variable is 0 and the standard deviation is 1. We tested cluster values of 1-14 and found that 3 clusters was the ideal based on a 'elbow plot' (Figure S15). The algorithm to do the cluster analysis is provided in the GitHub repository in *cluster_analysis.py*.

For each cluster, to generate the STIM relationship, we again used the median values of the runoff and variability parameters for the respective cluster, but keep k_e fixed to the median of the entire population. Cluster 1 (Very-low variability and moderate runoff) and Cluster 2 (Low variability and moderate runoff) are moderately well explained by the resulting STIM relationships, however Cluster 3 (High runoff) is not (Figure S17).

We can compare the relative performance of the clustered STIM relationships vs the whole population median STIM relationship by comparing the predicted vs observed erosion rates implied by each (Figure S18). To generate the ranges in predicted erosion rates, we used the standard deviations of the clustered populations of mean runoff and variability as uncertainty bounds for calculating implied erosion rates. For this, we assumed that higher mean runoffs would tend to be characterized by lower variability (higher values of k) and vice versa, i.e. the bounds on predicted erosion rates are constructed by pairing the upper bounds of R and k and pairing the lower bounds of R and k . We did not account for uncertainty on k_e in this analysis. We performed this either using the STIM relationship implied by the respective cluster (Left panel of Figure S18) or by the population median STIM relationship (Right panel of Figure S18). For the population median STIM relationships, the significantly larger error bars in predicted erosion rate reflect the larger magnitude of standard deviations on R and k for the whole population. While neither is perfect, for the majority of the data (excluding those in Cluster 3), the clustered STIM relationship is a better (Cluster 2) or similar (Cluster 1) predictor of erosion rates.

3 Supplemental Table Captions

Tables are provided as excel files as supplementary documents. The data in these tables are reproduced as text files (though spread across a wider number of files) in the GitHub repository. Below we provide captions for the supplementary tables referenced in the main text and this document.

3.1 Table S1

Summary of topographic, rainfall, and discharge statistics for gauged basins from the Global Runoff Data Centre (GRDC).

3.2 Table S2

Location of all samples collected in the Caucasus region and the result of these samples (either Data, indicating that we report a ^{10}Be erosion rate for this basin, Failed with reason for failure specified, or Not Analyzed).

3.3 Table S3

Master table reporting data for the basins for which we report ^{10}Be erosion rates. This excel table has multiple sheets, including Topography, Climate, Lithology, Quartz Masses, Be Measurements, Be Blanks, CRONUS v3 Inputs, Main Erosion Rates, CROSNSU v3 Litho Inputs, Litho Erosion Rates, CRONUS v3 Low Z Inputs, Low Z Erosion Rates, CRONUS v3 High Z Inputs, High Z Erosion Rates. The first sheet contains a readme with descriptions of each sheet.

4 Supplemental Figures and Captions

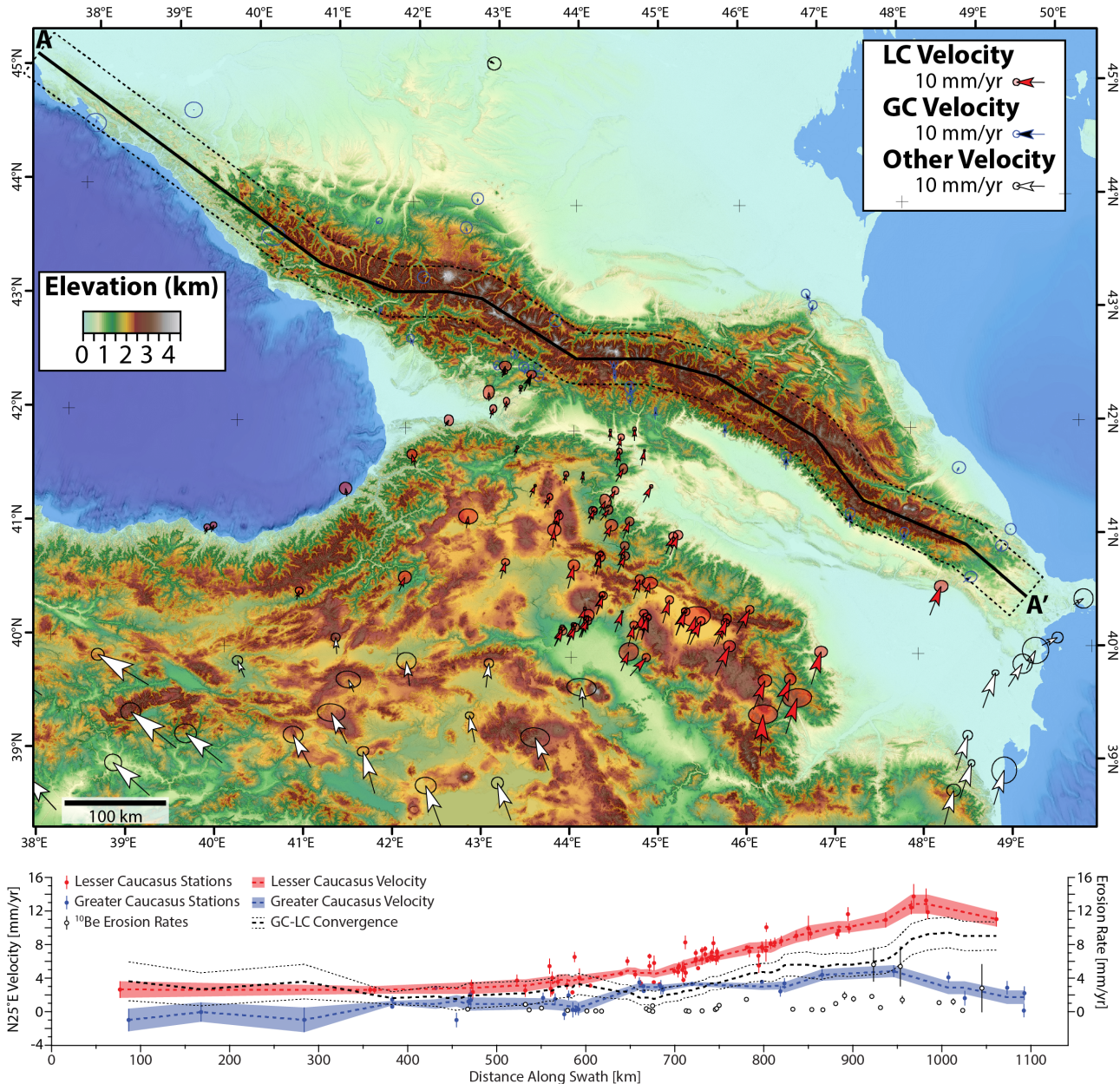


Figure S1: GPS stations within the Greater Caucasus regions from Reilinger et al. [2006], Kadirov et al. [2012], Sokhadze et al. [2018]. GPS swath is the same as in Figure 1.

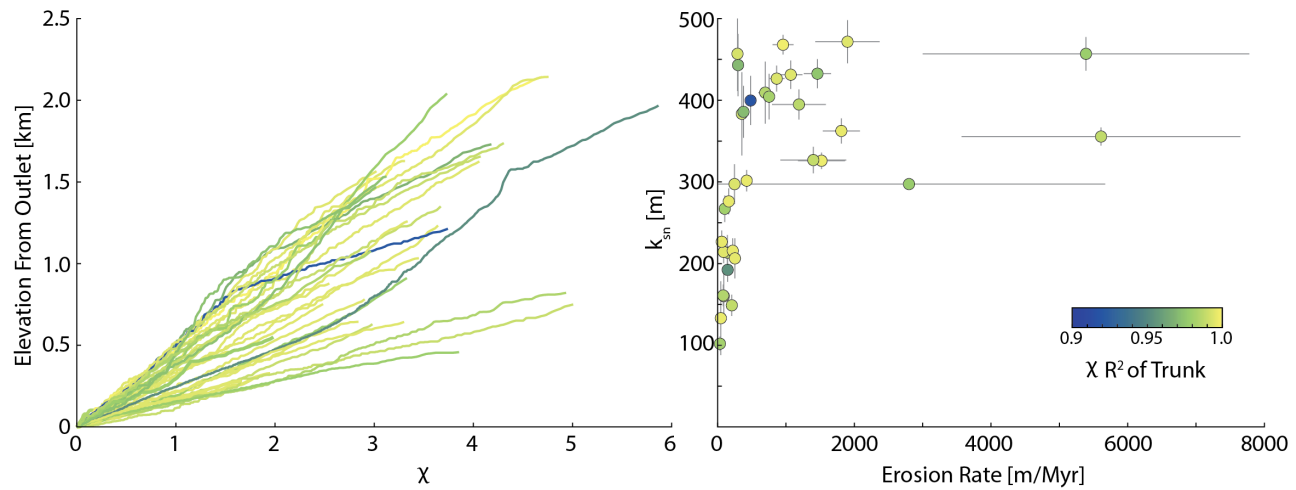


Figure S2: χ - elevation plots of the trunk streams of individual basins colored by the χR^2 of the trunk stream, and k_{sn} vs erosion rate colored by the χR^2 of the trunk stream.

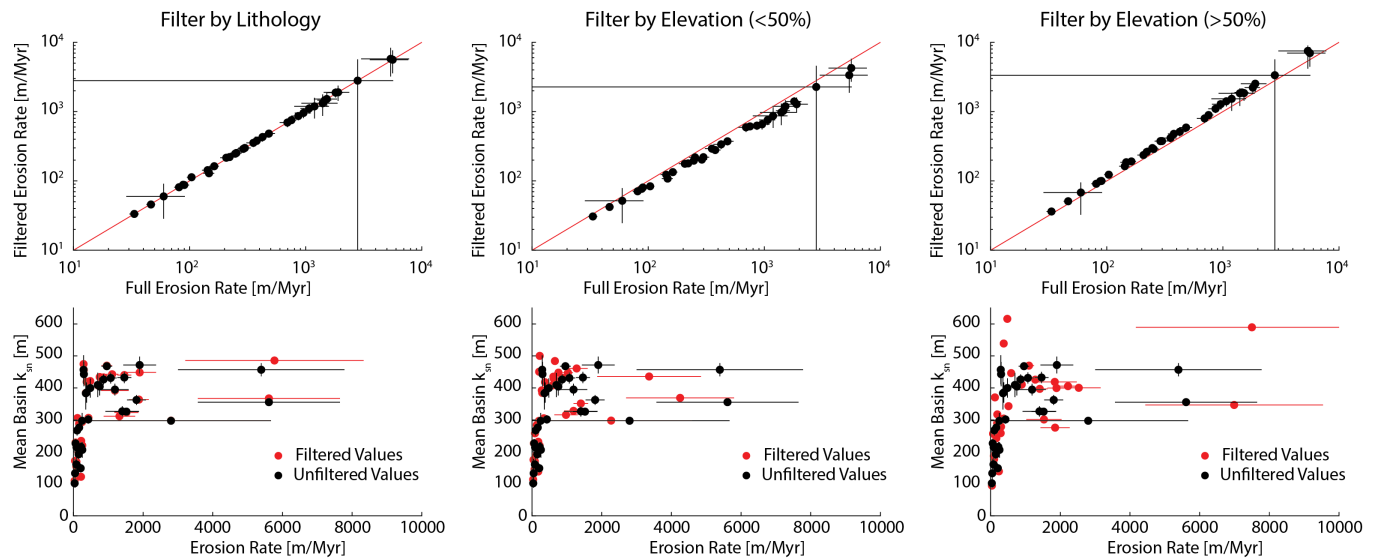


Figure S3: Comparison between erosion rates and mean basin k_{sn} as used in the main text and three different strategies for assessing the sensitivity to quartz sourcing.

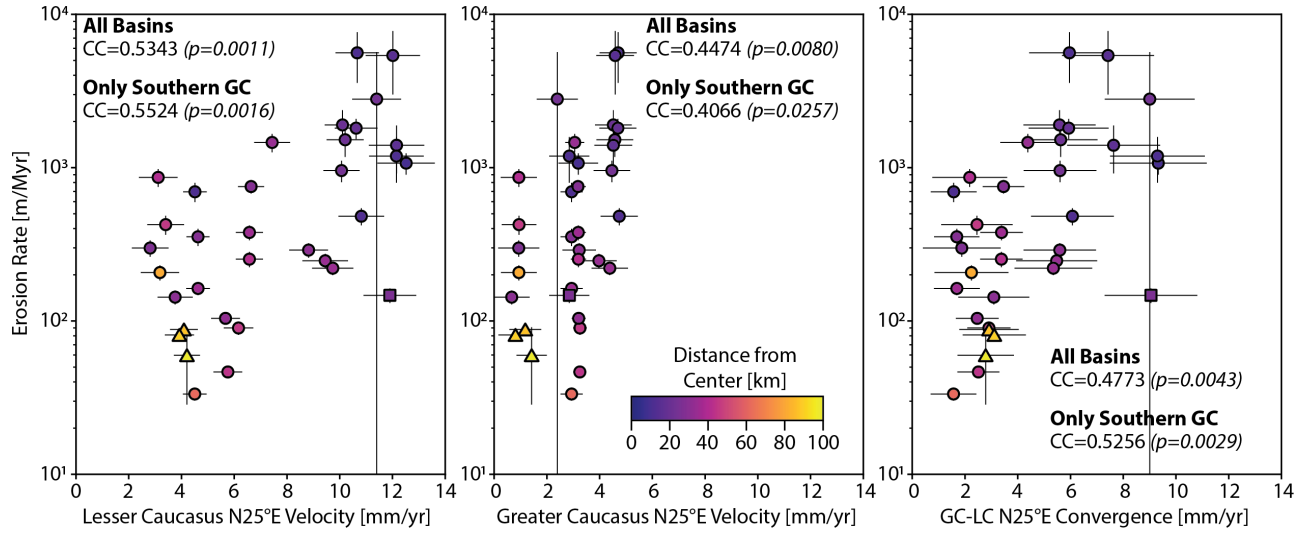


Figure S4: Comparison between Lesser Caucasus N25°E velocity (left), Greater Caucasus N25°E velocity (center), convergence between the Greater and Lesser Caucasus (right), and ¹⁰Be erosion rates. Square basin is in the northern Greater Caucasus and triangle basins are in the Lesser Caucasus. Correlation coefficients (CC) and corresponding p values are shown for the respective relationships.

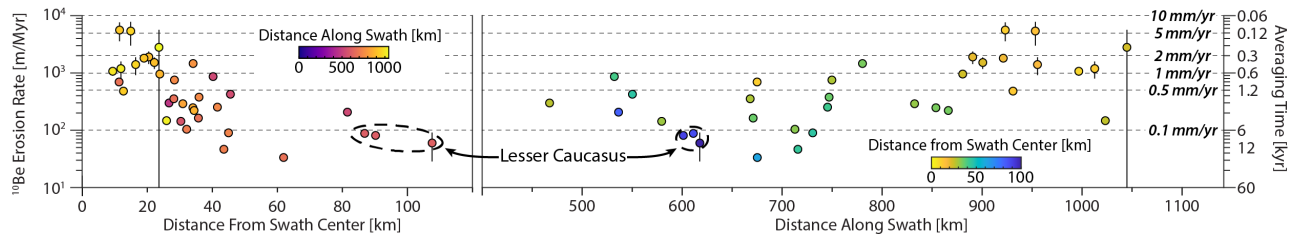


Figure S5: Erosion rate basins and their position along the swath (right) and from the center line of the swath (left), which approximates the topographic crest of the range.

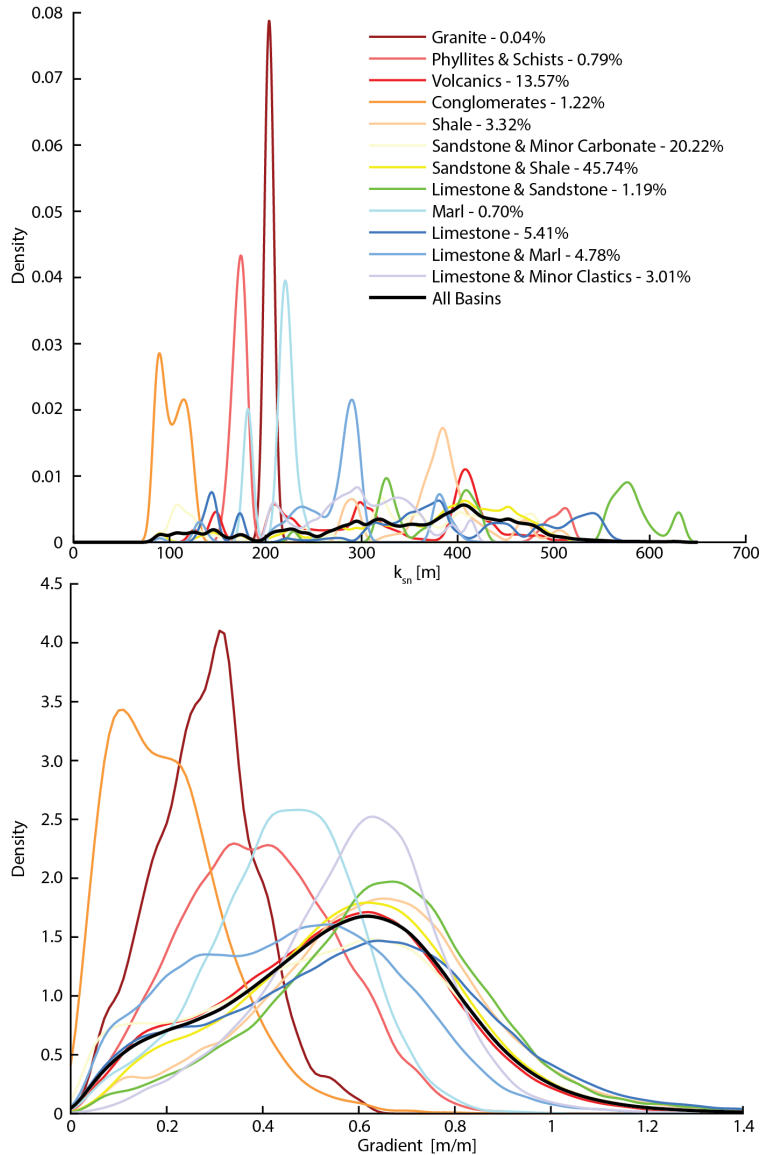


Figure S6: Kernel density estimates of k_{sn} (top) and gradient within specific lithologies. Percentages within explanation represent the fraction of the area within the entire population of sampled watersheds occupied by that lithology.

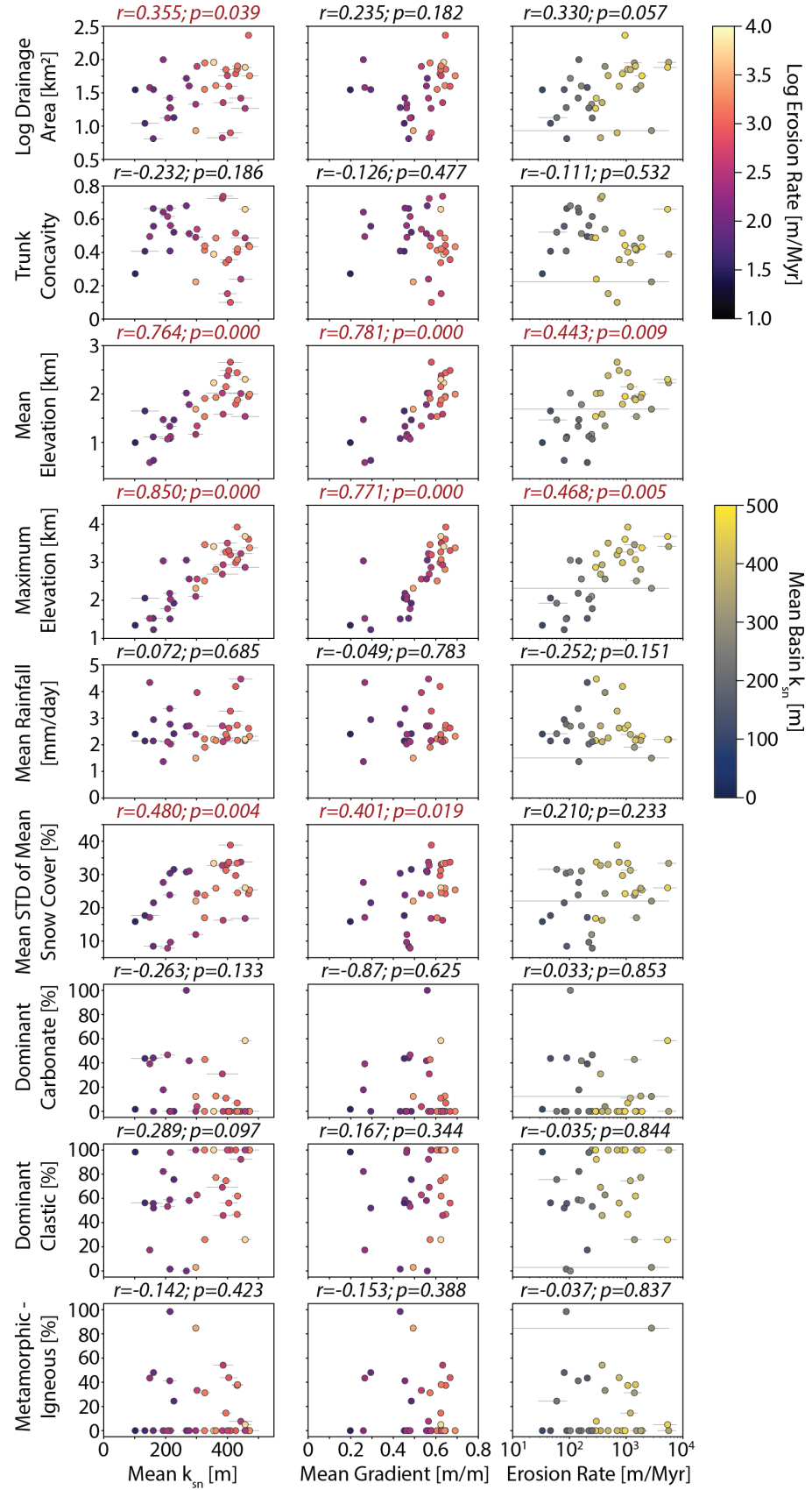


Figure S7: Comparisons of mean basin k_{sn} (left column), gradient (center column), and ^{10}Be (right column) against various other values. Pearson's correlation coefficient and significance (p-value) are shown for each relationship, those colored in red indicate a p value suggesting the relationship between the two variable is significant at the 95% confidence level.

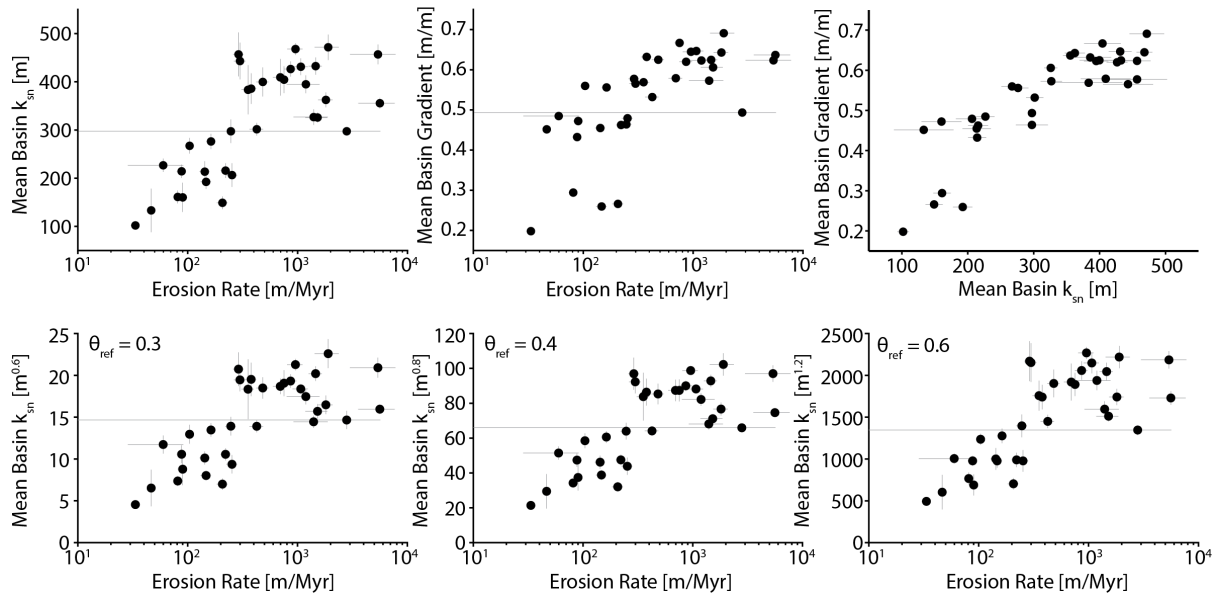


Figure S8: Top row shows basic relationships between k_{sn} , gradient and ^{10}Be erosionr rates. Bottom row shows k_{sn} - ^{10}Be relationships with k_{sn} calculated at different θ_{ref} values.

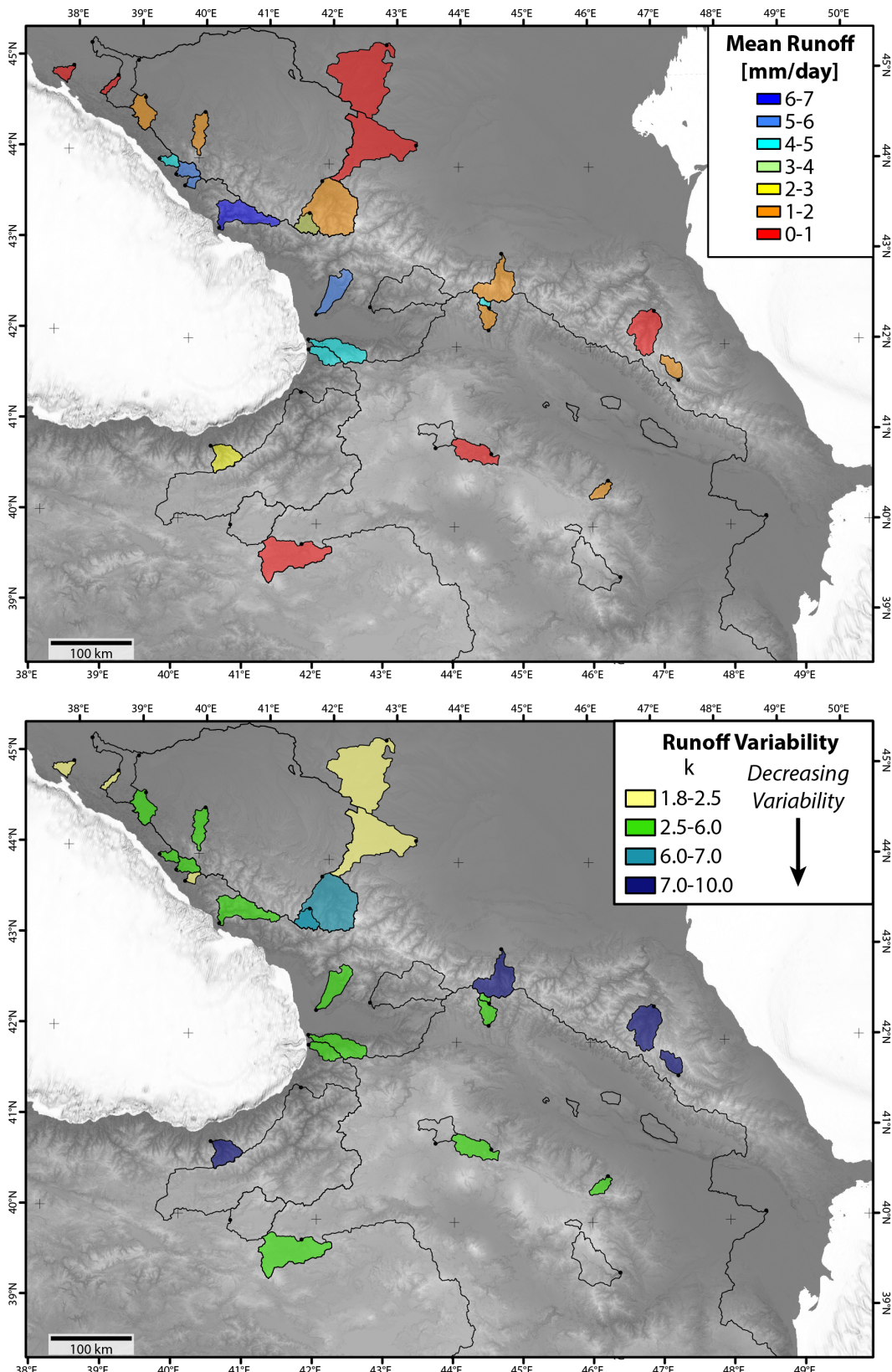


Figure S9: Upper: Mean daily runoff for GRDC basins used in this analysis. Basins without coloring are GRDC watersheds removed due to the presence of dams. Lower: Power law right tail (i.e. inverse gamma, k) of runoff distributions to characterize variability.

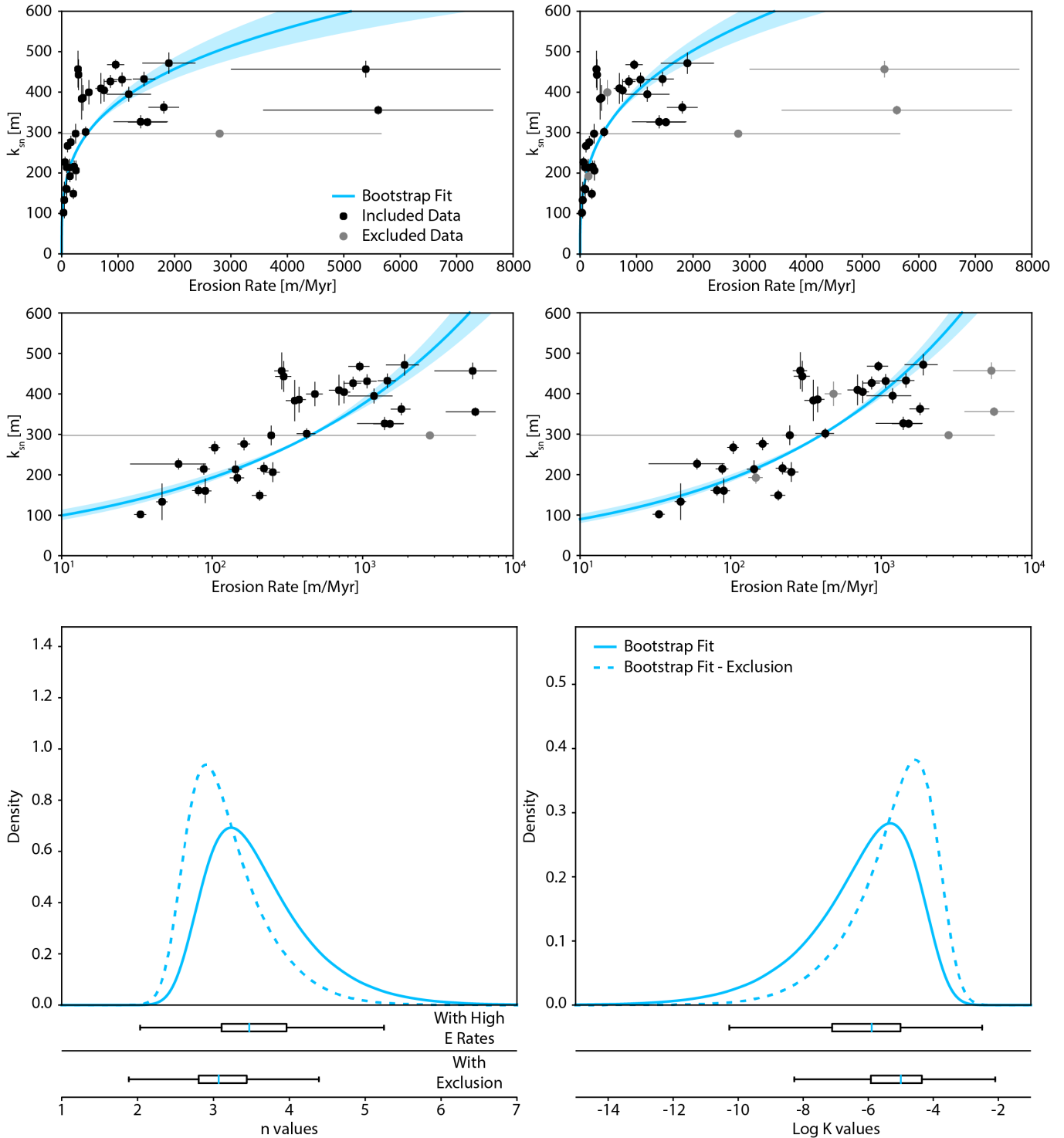


Figure S10: Power law fits to the data using a log-transformed version of the relationship and the bootstrap fitting method. Fits excluding the two highest erosion rate basins are also included. Box and whisker plots show median value with the colored line (which is used for the solid line relationship in plots above) and extent boxes represent the 25th and 75th percentiles (which are used to define the shaded regions in plots above).

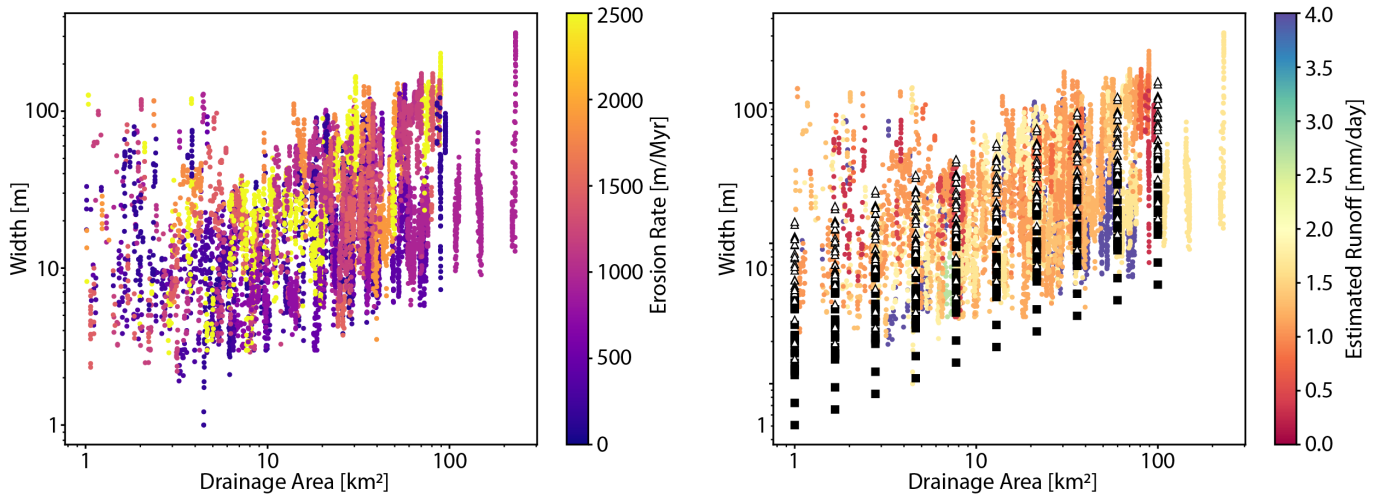


Figure S11: Comparison between widths measured on remotely sensed data and implied widths based on the choice of ω_a and k_w .

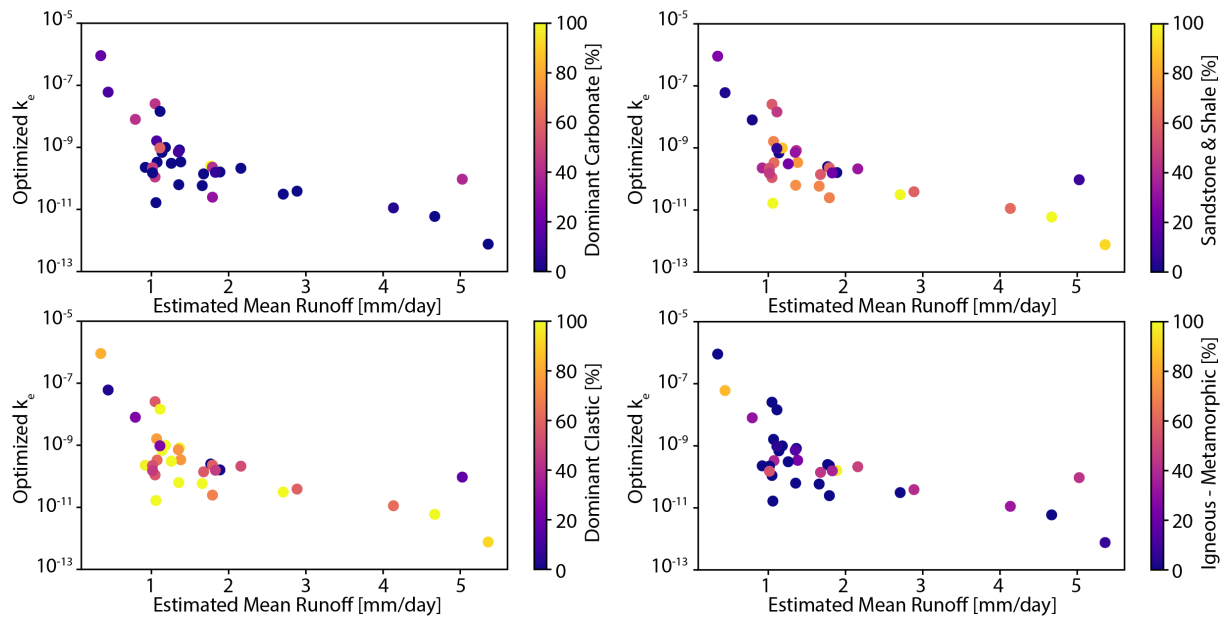


Figure S12: Variation of optimized k_e , R and lithology.

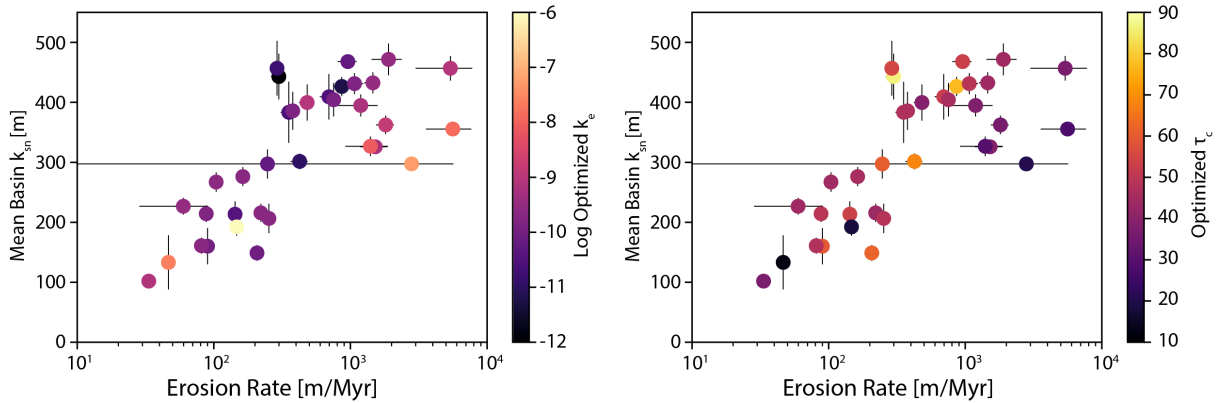


Figure S13: Relationship between k_{sn} , erosion rate, and optimized k_e and τ_c .

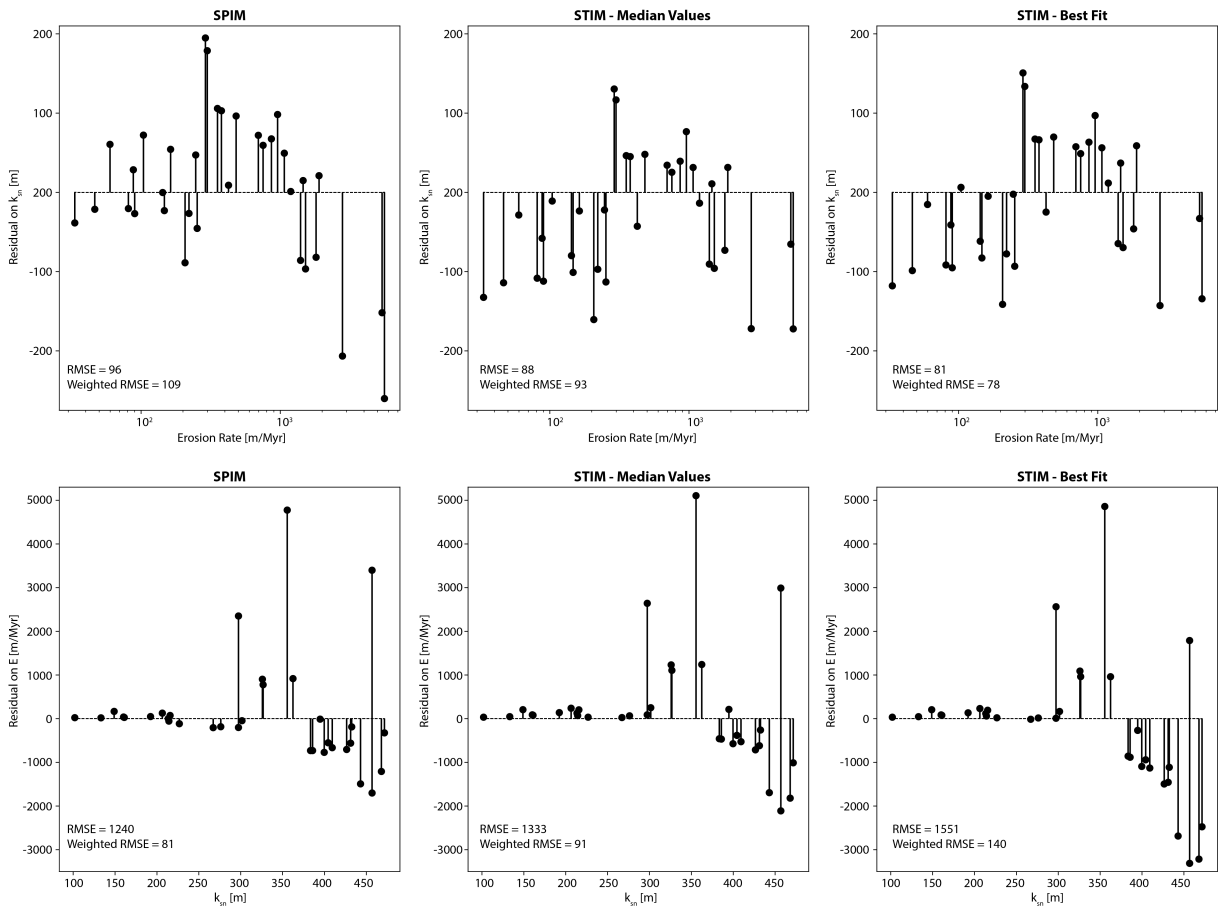


Figure S14: Comparisons of the residuals for the bootstrap SPIM fit (left column), the STIM median values relationship (center column), and the STIM ODR fit (right column). Residuals are calculated for both k_{sn} and erosion rate. Values for root mean square error (RMSE) and weighted RMSE, which considers the uncertainty on individual observations, are also shown.

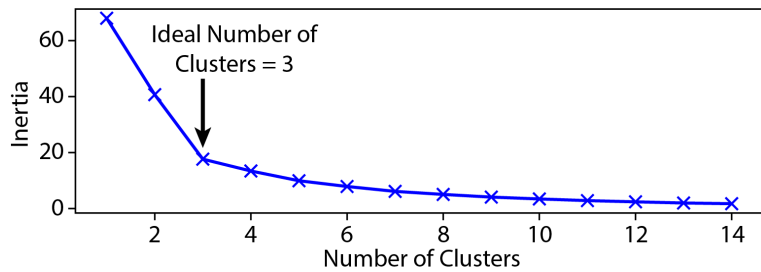


Figure S15: Elbow plot for determining ideal number of clusters in kmeans clustering of variability and runoff data.

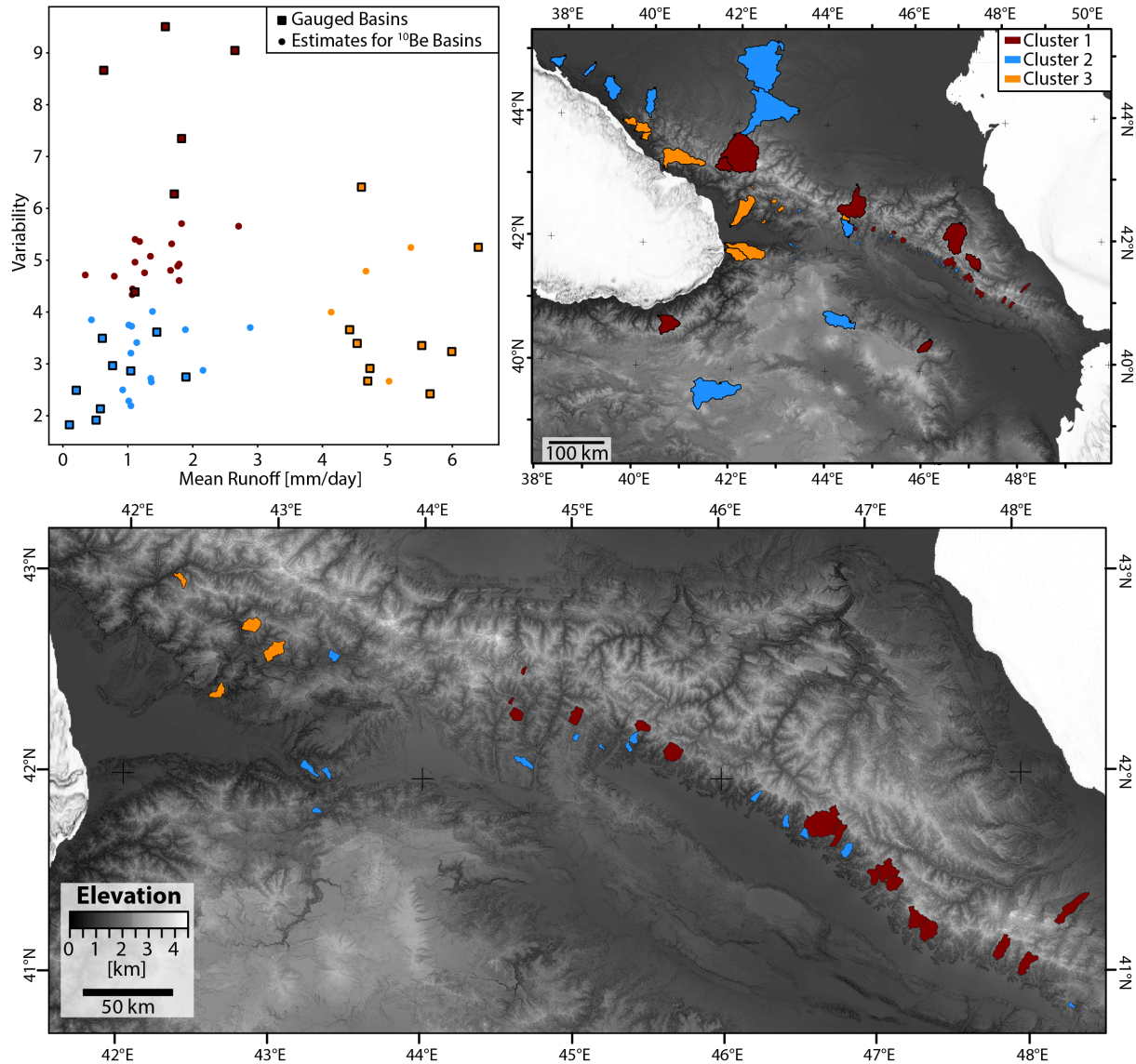


Figure S16: Upper left: Mean runoff versus variability for the GRDC gauged basins (squares) and th estimated parameters for the erosion rate basins, colored by their cluster membership. Upper right: Map of both GRDC basins and erosion rate basins colored by their cluster membership. Lower: Map of erosion rate basins colored by their cluster membership.

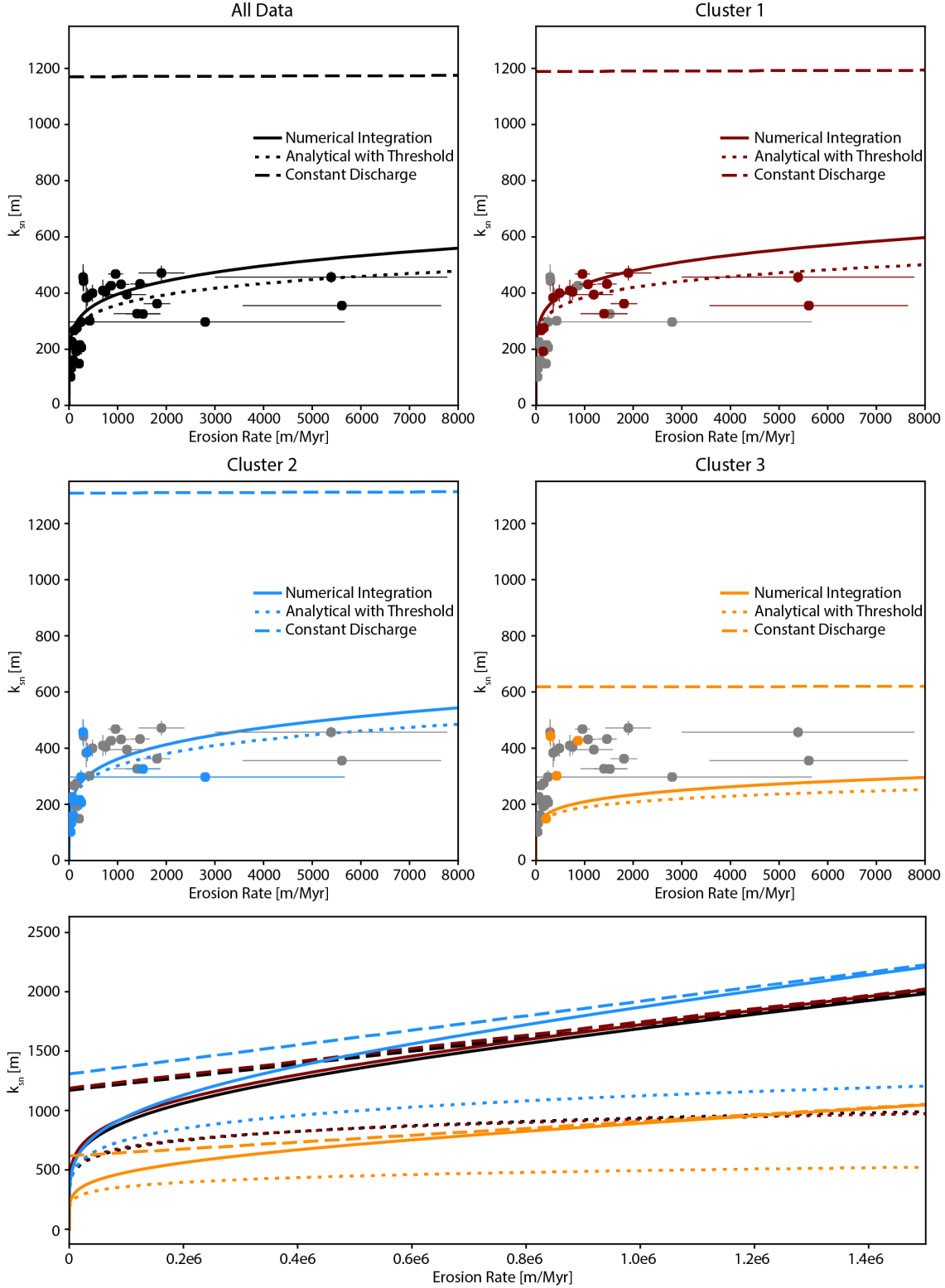


Figure S17: Relationship between k_{sn} and erosion rates and the predicted relationships based on STIM estimation using the entire dataset or specific clusters. Solid lines show the relationships as they appear in the main text, numerically solving equation S4, short dashed lines show solution using same parameters but the analytical approximation when thresholds are very large, long dashed lines show solution using same parameters but assuming constant discharge, refer to Lague et al. [2005] for the relevant equations for these alternative solutions

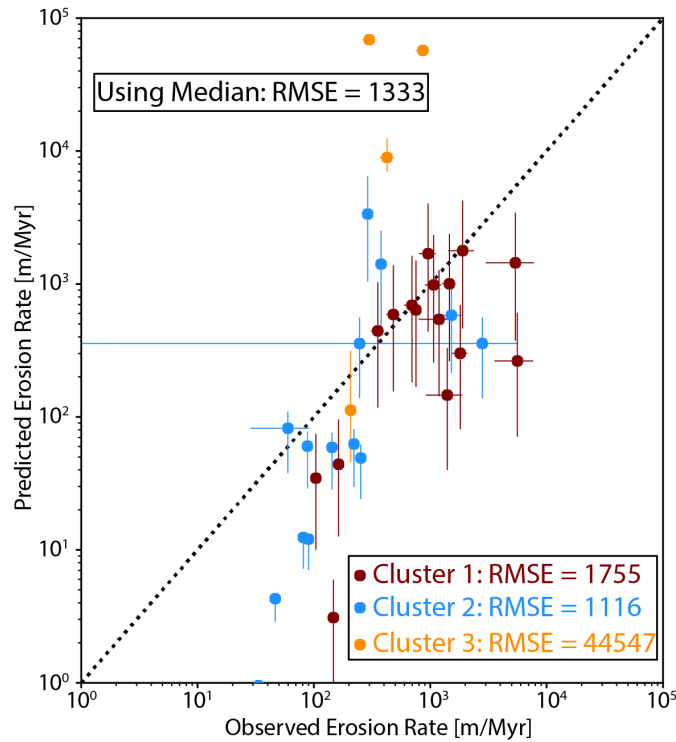


Figure S18: Difference between observed erosion rate (i.e. ^{10}Be erosion rate) and predicted erosion rate for individual basins using the STIM relationship for the respective cluster to which that basin belongs. As in the main text, k_e is held fixed to the same value as the whole population. The corresponding RMSE if using the median relationship is also reported. RMSE are calculated for the residual on erosion rate.

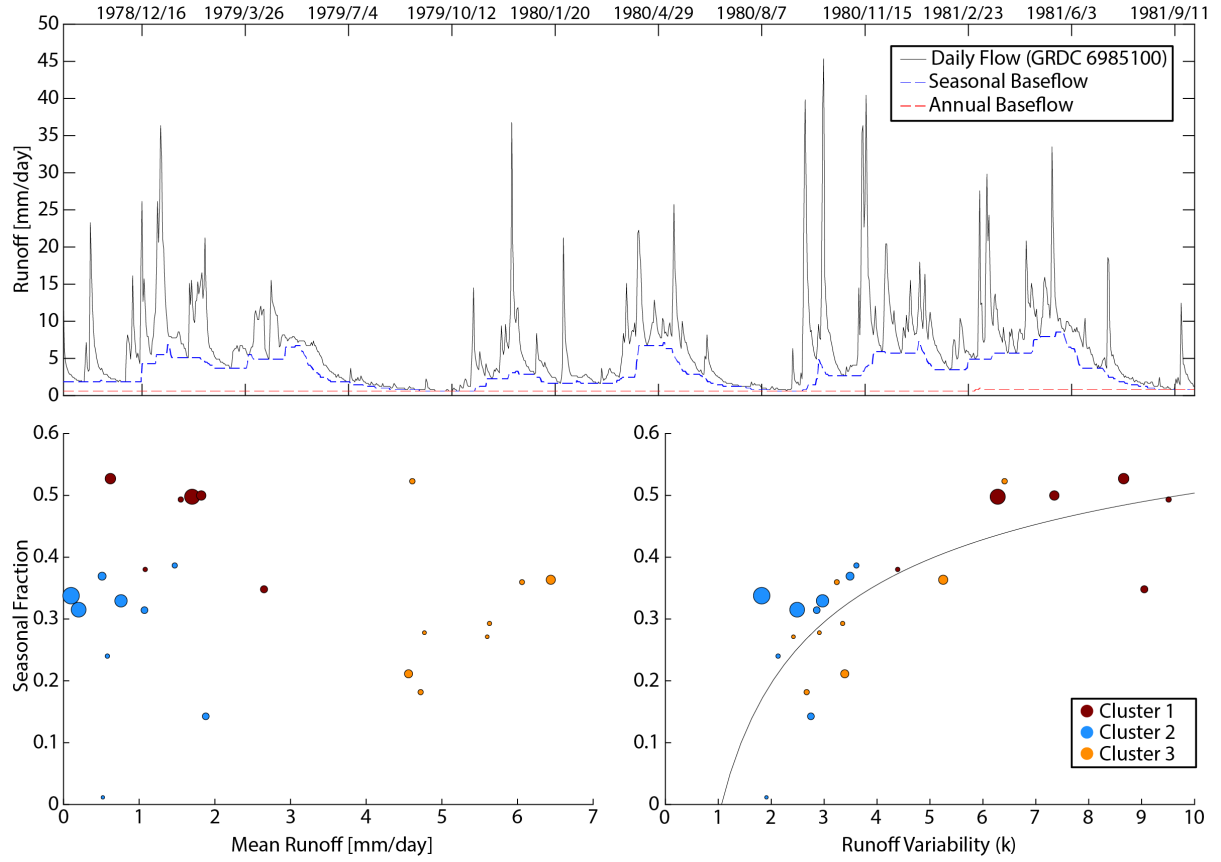


Figure S19: Upper: Example event , seasonal , and annual component separation. Bottom: Relationship between seasonal runoff fraction and (left) mean runoff and (right) runoff variability. Points on bottom plots are scaled by drainage area and color-coded by results from k-means clustering analysis from Figure 9 in main text.

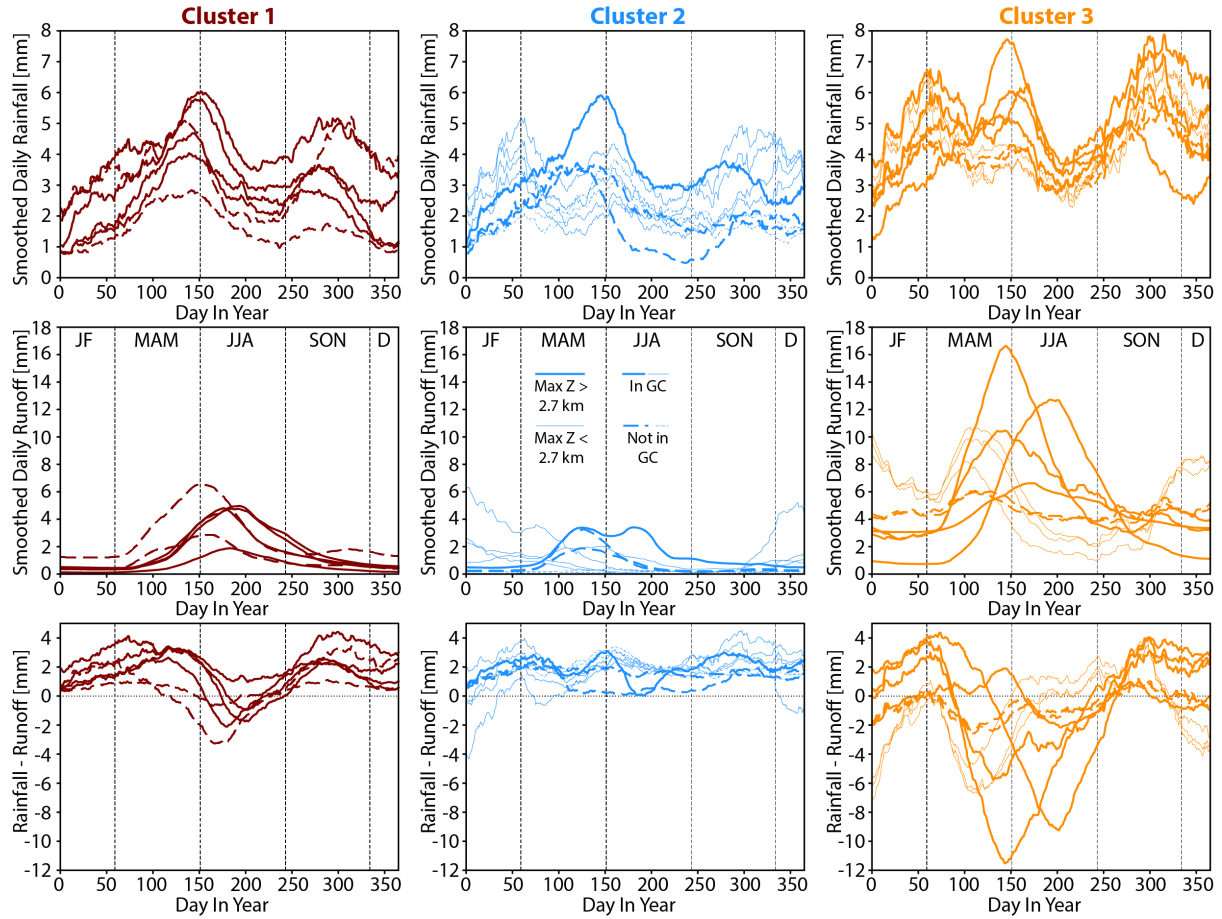


Figure S20: Upper: Averaged and smoothed rainfall time series, Middle: Averaged and smoothed runoff time series, and Bottom: Rainfall-Runoff. Watersheds are broken up by cluster from k-means clustering analysis from Figure 9 in main text. Meaningful differences in patterns were found if the data was filtered between watersheds with a maximum elevation greater or less than 2.7 km

References

- Byron A. Adams, Kelin X. Whipple, Adam M. Forte, Arjun M. Heimsath, and Kip V. Hodges. Climate controls on erosion in tectonically active landscapes. *Science Advances*, 6(42), 2020. doi: 10.1126/sciadv.aaz3166.
- A A Ali-Zade. Geological Map of Azerbaijan Republic, 2005.
- Akif A. Alizadeh, Ibrahim S. Guliyev, Fakhraddin A. Kadirov, and Lev V. Eppelbaum. *Geosciences of Azerbaijan: Volume I: Geology*. Regional Geology Reviews. Springer International Publishing, Cham, 2016. ISBN 978-3-319-27393-8 978-3-319-27395-2. doi: 10.1007/978-3-319-27395-2.
- Boris Avdeev and Nathan A Niemi. Rapid Pliocene exhumation of the central Greater Caucasus constrained by low-temperature thermochronometry. *Tectonics*, 30, 2011. doi: 10.1029/2010TC002808.
- Greg Balco, J Stone, N A Lifton, and Tibor Dunai. A complete and easily accessible means of calculating surface exposure ages or erosion rates from ^{10}Be and ^{26}Al measurements. *Quaternary Geochronology*, 3:174–195, 2008. doi: 10.1016/j.quageo.2007.12.001.
- Roman A. DiBiase. Short Communication: Increasing vertical attenuation length of cosmogenic nuclide production on steep slopes negates topographic shielding corrections for catchment erosion rates. Preprint, Cross-cutting themes: Geochronology applied to establish timing and rates of Earth surface processes, July 2018.
- Roman A DiBiase and Kelin X Whipple. The influence of erosion thresholds and runoff variability on the relationships among topography, climate, and erosion rate. *Journal of Geophysical Research*, 116(F04036), 2011. doi: 10.1029/2011JF002095.
- R.G. Ditchburn and N.E. Whitehead. The separation of ^{10}Be from silicates. In *3rd Workshop of the South Pacific Environmental Radioactivity Association*, pages 4–7, 1994.
- A I Dzhanelidze and N A Kandelaki. K-38-XIII, 1957.
- G. Burch Fisher, Bodo Bookhagen, and Colin B. Amos. Channel planform geometry and slopes from freely available high-spatial resolution imagery and DEM fusion: Implications for channel width scalings, erosion proxies, and fluvial signatures in tectonically active landscapes. *Geomorphology*, 194:46–56, 2013. ISSN 0169-555X. doi: 10.1016/j.geomorph.2013.04.011.
- Adam M Forte and Kelin X Whipple. Short communication : The Topographic Analysis Kit (TAK) for TopoToolbox. *Earth Surface Dynamics*, 7:87–95, 2019. doi: 10.5194/esurf-7-87-2019.
- Adam M Forte, Eric Cowgill, and Kelin X Whipple. Transition from a singly vergent to doubly vergent wedge in a young orogen: The Greater Caucasus. *Tectonics*, 33(11):2077–2101, 2014. doi: 10.1002/2014TC003651.
- Adam M Forte, Kelin X Whipple, B Bookhagen, and Matthew W Rossi. Decoupling of modern shortening rates, climate, and topography in the Caucasus. *Earth and Planetary Science Letters*, 449:282–294, 2016. doi: 10.1016/j.epsl.2016.06.013.
- P D Gamkrelidze. K-38-XX, 1958.
- P D Gamkrelidze and I R Kakhazdze. K-38-VII, 1959.
- Ramin Gobejishvili, Nino Lomidze, Levan Tielidze, and Jaap J M van der Meer. Late Pleistocene (Würmian) Glaciations of the Caucasus. In J Ehlers, P L Gibbard, and P D Hughes, editors, *Quaternary Glaciations - Extent and Chronology*, pages 141–147. Elsevier, Amsterdam, 2011.
- Fakhraddin Kadirov, Michael Floyd, Akif Alizadeh, Ibrahim Guliev, R Reilinger, Sadi Kuleli, R King, and M N Toksoz. Kinematics of the eastern Caucasus near Baku, Azerbaijan. *Natural Hazards*, 63:997–1006, 2012.
- D N Kandelaki and I R Kakhadze. K-38-XV, 1957.
- N A Kandelaki and I R Kakhadze. K-38-XIV, 1957.
- V E Khain and A N Shardanov. K-39-XXV, 1960.

A. M. G. Klein Tank, J. B. Wijngaard, G. P. Können, R. Böhm, G. Demarée, A. Gocheva, M. Mileta, S. Pashiardis, L. Hejkrlik, C. Kern-Hansen, R. Heino, P. Bessemoulin, G. Müller-Westermeier, M. Tzanakou, S. Szalai, T. Pálssdóttir, D. Fitzgerald, S. Rubin, M. Capaldo, M. Maugeri, A. Leitass, A. Bukanis, R. Aberfeld, A. F. V. van Engelen, E. Forland, M. Mietus, F. Coelho, C. Mares, V. Razuvayev, E. Nieplova, T. Cegnar, J. Antonio López, B. Dahlström, A. Moberg, W. Kirchhofer, A. Ceylan, O. Pachaliuk, L. V. Alexander, and P. Petrovic. Daily dataset of 20th-century surface air temperature and precipitation series for the European Climate Assessment: EUROPEAN TEMPERATURE AND PRECIPITATION SERIES. *International Journal of Climatology*, 22(12):1441–1453, October 2002. ISSN 08998418. doi: 10.1002/joc.773.

C. Kohl and K. Nishizumi. Chemical isolation of quartz for measurement of in situ-produced cosmogenic nuclides. *Geochimica et Cosmochimica Acta*, 56(9):3583–3587, 1992.

V N Krestnikov. K-38-XVI, 1957.

Dimitri Lague, N Hovius, and P Davy. Discharge, discharge variability, and the bedrock channel profile. *Journal of Geophysical Research*, 110:F04006–F04006, 2005. doi: 10.1029/2004JF000259.

V A Melnikov and E I Popova. K-38-VIII, 1975.

Charles Mifsud, Toshiyuki Fujioka, and David Fink. Extraction and purification of quartz in rock using hot phosphoric acid for in situ cosmogenic exposure dating. *Nuclear Instruments and Methods in Physics Research B*, 294:203–207, 2013. ISSN 0168-583X. doi: 10.1016/j.nimb.2012.08.037.

Nathan A Niemi, Michael Osokin, Douglas Burbank, Arjun M Heimsath, and Emmanuel J Gabet. Effects of bedrock landslides on cosmogenically determined erosion rates. *Earth and Planetary Science Letters*, 237:480–498, 2005.

M. C. Palucis and M. P. Lamb. What controls channel form in steep mountain streams?: Controls on Steep Channel Form. *Geophysical Research Letters*, 44(14):7245–7255, July 2017. ISSN 00948276. doi: 10.1002/2017GL074198.

Eric W Portenga and Paul R Bierman. Understanding Earth's eroding surface with ^{10}Be . *GSA Today*, 21(8):4–10, 2011. doi: 10.1130/G111A.1.

R Reilinger, S McClusky, Philippe Vernant, S Lawrence, S Ergintav, Rahsan Cakmak, Haluk Ozener, Fakhreddin Kadirov, Ibrahim Guliev, Ruben Stepanyan, M Nadariya, Galaktion Hahubia, S Mahmoud, K Sakr, Abdullah ArRajehi, D Paradissis, A Al-Aydrus, M Prilepin, Tamara Guseva, Emre Evren, Andriy Dmitrotsa, S V Filikov, Francisco Gomez, Riad Al-Ghazzi, and Gebran Karam. GPS constraints on continental deformation in the Africa-Arabia-Eurasia continental collision zone and implications for the dynamics of plate interactions. *Journal of Geophysical Research*, 111:doi:10.1029/2005JB004051–doi:10.1029/2005JB004051, 2006.

Joshua J Roering, J Taylor Perron, and James W Kirchner. Functional relationships between denudation and hillslope form and relief. *Earth and Planetary Science Letters*, 264:245–258, 2007.

Matthew W Rossi, Kelin X Whipple, and Enrique R Vivoni. Precipitation and evapotranspiration controls on event-scale runoff variability in the contiguous United States and Puerto Rico. *Journal of Geophysical Research*, 121, 2016. doi: 10.1002/2015JF003446.

W Schwanghart and D Scherler. Short Communication: TopoToolbox 2 - MATLAB based software for topographic analysis and modeling in Earth surface sciences. *Earth Surface Dynamics*, 2:1–7, 2014. doi: 10.5194/esurf-2-1-2014.

G. Sokhadze, M. Floyd, T. Godoladze, R. King, E. S. Cowgill, Z. Javakhishvili, G. Hahubia, and R. Reilinger. Active convergence between the Lesser and Greater Caucasus in Georgia: Constraints on the tectonic evolution of the Lesser–Greater Caucasus continental collision. *Earth and Planetary Science Letters*, 481:154–161, 2018. doi: 10.1016/j.epsl.2017.10.007.

John O. Stone. Air pressure and cosmogenic isotope production. *Journal of Geophysical Research: Solid Earth*, 105(B10): 23753–23759, October 2000. ISSN 01480227. doi: 10.1029/2000JB900181.

J. V. Sutcliffe, F. A. K. Farquharson, E. L. Tate, and S. S. Folwell. Flood regimes in the Southern Caucasus: The influence of precipitation on mean annual floods and frequency curves. *Hydrology Research*, 39(5-6):385–401, October 2008. ISSN 0029-1277, 2224-7955. doi: 10.2166/nh.2008.025.

Gregory E Tucker. Drainage basin sensitivity to tectonic and climatic forcing: Implications of a stochastic model for the role of entrainment and erosion thresholds. *Earth Surface Processes and Landforms*, 29:185–204, 2004. doi: 10.1002/esp.1020.

Gregory E Tucker and Rafael L Bras. A stochastic approach to modeling the role of rainfall variability in drainage basin evolution. *Water Resources Research*, 36(7):1953–1964, 2000.

H Wulf, B Bookhagen, and D Scherler. Differentiating between rain, snow, and glacier contributions to river discharge in the western Himalaya using remote-sensing data and distributed hydrologic modeling. *Advances in Water Resources*, 88: 152–169, 2016. doi: 10.1016/j.advwatres.2015.12.004.

B J Yanites, Gregory E Tucker, and Robert S Anderson. Numerical and analytical models of cosmogenic radionuclide dynamics in landslide-dominated drainage basins. *Journal of Geophysical Research*, 114:F01007–F01007, 2009. doi: 10.1029/2008JF001088.

Brian J. Yanites, Nate A. Mitchell, Joshua C. Bregy, Grace A. Carlson, Kirstyn Cataldo, Margaret Holahan, Graham H. Johnston, Amelia Nelson, Jeffery Valenza, and Matthew Wanker. Landslides control the spatial and temporal variation of channel width in southern Taiwan: Implications for landscape evolution and cascading hazards in steep, tectonically active landscapes: Variation in channel morphology controlled by landslides in s. Taiwan. *Earth Surface Processes and Landforms*, 43 (9):1782–1797, July 2018. ISSN 01979337. doi: 10.1002/esp.4353.